

# Elastic plastic self-consistent (EPSC) modeling of San Carlos olivine deformed in a D-DIA apparatus <sup>♠</sup>

PAMELA C. BURNLEY<sup>1,\*</sup> AND SHIRIN KABOLI<sup>1</sup>

<sup>1</sup>Department of Geoscience and High Pressure Science and Engineering Center, University of Nevada Las Vegas (UNLV), Las Vegas, Nevada 89154-4010, U.S.A.

## ABSTRACT

We present a suite of low strain deformation experiments conducted on polycrystalline San Carlos olivine in a deformation DIA apparatus at temperatures ranging from 440 to 1106 °C at pressures between 3.8 and 4.6 GPa. The deformation behavior was monitored using in situ diffraction of white synchrotron X-rays. The experiments were conducted at a slow strain rate of  $\sim 5 \times 10^{-6}$ /s so as to allow the initial elastic behavior to be closely monitored. For each experiment, we fit the diffraction data using elastic plastic self-consistent (EPSC) models. We find that to model the experiments we must incorporate an isotropic deformation mechanism that permits a small amount of non-elastic deformation during the initial elastic portion of the experiment. This deformation mechanism mimics the observed reduction in the elastic modulus as a function of temperature and permits us to better model the remainder of the stress strain curve. The critical resolved shear stresses (CRSS) for slip obtained from these models compare well with those measured in single-crystal deformation experiments

**Keywords:** High-pressure studies, olivine, deformation, XRD data, synchrotron X-ray, diffraction

## INTRODUCTION

The advent of synchrotron-based high-pressure deformation experiments has produced significant advances in our understanding of deformation in Earth's deep interior. However, methods for measuring the bulk strength of materials from X-ray powder diffraction data with certainty are still lacking (Jain et al. 2017). Most investigators use the difference between *d*-spacings measured in the compressional and transverse directions combined with the diffraction elastic constants (Singh et al. 1998) to calculate the stress state in their samples. The method assumes a Reuss state of stress in the material, but the stresses given by different reflections can vary widely (cf. Burnley and Zhang 2008; Mei et al. 2010). The average of the measured stresses is typically used, however the resulting average depends upon which diffraction lines the experimenter happens to measure. Significant success has been achieved with elastic plastic self-consistent (EPSC) modeling that has been used extensively to interpret neutron and X-ray diffraction from deforming metals (Turner and Tome 1994; Turner et al. 1995; Agnew et al. 2006; Merkel et al. 2009) as well as X-ray diffraction from in situ deformation experiments on MgO (Li et al. 2004), quartz (Burnley and Zhang 2008), alumina (Raterron et al. 2013; Kaboli and Burnley 2017), and olivine (Hilaireret et al. 2012; Burnley 2015; Kaboli et al. 2017). EPSC models simulate the response of crystals based on their orientation with respect to the loading boundary conditions, and they include groups of grains (grain populations) observed by diffraction as well as the mechanical contribution of “silent” grains that are not participating in produc-

ing diffraction. However, finding EPSC fits for diffraction from olivine deforming at high temperature has been more challenging (Hilaireret et al. 2012). We have shown (Burnley 2015; Kaboli et al. 2017) that including a kink band deformation mechanism to close the yield surface produces more satisfactory EPSC models, however modeling the slope of olivine stress-strain curves at low strain remains a challenge especially at high temperature (cf. Hilaireret et al. 2012).

The motivation to examine low strain behavior is twofold. First, if one is going to use a forward modeling strategy such as EPSC to interpret diffraction from in situ deformation it would be most desirable for the model to match the evolution of stress in the sample from the start rather than deviating significantly early on and then trying to match the experimental results at higher strain levels. Second, the process governing the early evolution of stress and strain during deformation are important in their own right, in that these processes govern the initial distribution of stress and strain throughout the body of the polycrystal and are probably also important for understanding phenomena such as transient creep.

Textbook descriptions as well as the EPSC model assume that materials behave elastically when the load is first applied. However, the elastic portion of typical stress-strain curves from compression experiments on polycrystalline materials generally do not reproduce what is predicted by the Young's modulus of the material as measured by other techniques. This discrepancy is often informally attributed by experimentalists to various instrumental effects that depend on where, relative to the sample, the load and displacement are measured. There is also the recognition that grain boundary effects may be involved in the apparent lowering of the modulus as it is in metals (Ke 1947), but due to the instrument effects, little attention has been paid to this phenomena.

\* E-mail: Pamela.Burnley@unlv.edu

<sup>♠</sup> Open access: Article available to all readers online.

In situ deformation experiments conducted with synchrotron X-rays offer the opportunity to explore low strain behavior further. Unlike standard laboratory deformation apparatus where the load and displacement are measured remotely from the sample via a load cell and displacement transducers, synchrotron X-ray diffraction techniques measure both the stress and strain directly from the sample (Vaughan et al. 2000; Weidner et al. 1998, 2010). Therefore, instrument effects should not exist (or at worse be of a substantially different variety). In this paper, we describe a series of low strain deformation experiments on San Carlos olivine performed at various temperatures. We chose a strain rate that was slow enough to collect many data points during the first 2% strain. We construct EPSC models to match our data and discuss the implications.

## METHODS

### D-DIA apparatus

The experiments described in this manuscript were conducted using the deformation DIA (D-DIA) apparatus (Durham et al. 2002; Wang et al. 2003; Weidner and Li 2006; Weidner et al. 2010) located at beamline 6BM-B at the Advanced Photon Source, Argonne National Laboratory, which utilizes a bending magnet that produces a white X-ray beam. The sample assembly (Supplemental<sup>1</sup> Fig. S1), based on the “sphere-in-seats design” (Durham et al. 2009); is described in detail in the supplementary section as well as in Kaboli et al. (2017). The sample consisted of a pulverized single crystal of San Carlos olivine in series with a fully dense Al<sub>2</sub>O<sub>3</sub> “inner piston” (Coors AD998) all enclosed in a 25 μm thick Ni metal jacket. A W-Re thermocouple was incorporated into the upper piston. Pt foils (25 μm thick) were placed at the top and bottom of the olivine specimen and at the bottom of the inner piston to measure the length of both from radiographs taken during the experiment.

The experiment was compressed to ~6 GPa at room temperature and annealed at 1200 °C for 3 h and 50 min. For experimental samples of San Carlos olivine produced in this fashion, we generally obtain an aggregate with various grain sizes ranging from 1–50 μm. For this particular experiment, we infer from the grain size distribution in the sample after the experiment (see Supplemental<sup>1</sup> Fig. S7) that the resulting initial grain size was around ~35 μm as is described in detail in the supplementary material. After annealing, the temperature was then lowered to the first experimental temperature. The combination of cell relaxation during annealing and thermal contraction on cooling reduces the experimental pressure from that observed during the initial compression considerably. X-ray spectra were collected at this initial condition and then the D-DIA inner rams were advanced to deform the specimen while in situ diffraction observations were made. The motor speed for the D-DIA ram pumps was chosen to produce a strain rate of ~5 × 10<sup>-6</sup>/s, a strain rate that would allow for good documentation of the low strain behavior of the sample. After several percent strain was achieved the motors for the inner D-DIA rams were stopped. The temperature was then raised to 1200 °C and the inner rams were retracted briefly at the rate of ~10<sup>-3</sup>/s to relax any remaining stresses. The temperature was then changed to the next experimental temperature and the next sequence begun. This sequence of short deformation experiments and relaxation periods was repeated for the four temperature conditions reported here. A fifth and final deformation sequence was conducted, but since during data analysis we found that the stress state was not fully relaxed before the start of the final sequence, that data was discarded.

**TABLE 1.** Experimental conditions for each deformation sequence

	Anneal temperature <sup>a</sup> (°C)	Anneal time (h:mm)	Temperature deformation <sup>a</sup> (°C)	Pressure <sup>b</sup> (GPa)	Strain rate ×10 <sup>-6</sup> /s	Strain
Sequence 1	1210.2 ± 3.9	3:48	440.5 ± 1.9	3.8 ± 0.1	2.5	3.47
Sequence 2	1192.9 ± 9.6	1:17	663.2 ± 2.5	4.3 ± 0.1	3.3	3.64
Sequence 3	1207.5 ± 2.7	0:23	882.3 ± 1.2	4.5 ± 0.1	4.3	3.09
Sequence 4	1198.9 ± 7.8	0:24	1106.4 ± 3.9	4.6 ± 0.1	4.7	2.77

<sup>a</sup> Uncertainty in temperature is based on observed temperature variation during experiment. As discussed in the supplementary material, we estimate the systematic uncertainty in temperature to be <3%.

<sup>b</sup> Uncertainty in pressure includes both uncertainty in measured *d*-spacings and temperature uncertainty.

No effort was made to adjust the experimental pressure beyond the automatic feedback system that keeps the oil pressure constant. Thus the pressure for each deformation sequence was somewhat different. Conditions for the deformation sequences and annealing times before each sequence are given in Table 1.

### In situ X-ray measurements

Radiographs of the sample and inner piston were taken at ~12 min intervals during deformation and the length of each was analyzed using Image-J (Schneider et al. 2012). Sample strain was calculated as

$$\epsilon = \frac{(l - l_0)}{l_0}$$

where *l* is the instantaneous sample length and *l*<sub>0</sub> is starting length of the sample, which was recorded at the pressure and temperature conditions of the experiment immediately before the D-DIA rams begun advancing for each deformation sequence. Sample strain measurements are not synchronous with the diffraction measurements; therefore, the sample strain associated with each diffraction measurement must be calculated. Since we typically observe some sluggishness in the system when deformation first begins, rather than calculating sample strain from a linear fit of all the sample strain vs. time data, we fit the data with a polynomial function (see supplementary section<sup>1</sup>). This is particularly important for characterizing the slope of the stress-strain curve at the lowest strains. Quoted strain rates (Table 1) are for the portion of the experiment after the sample strain vs. time behavior becomes linear.

### X-ray diffraction data analysis

Diffraction data for both the sample and the inner piston were taken at 6 min intervals throughout each deformation sequence. The experimental setup had 10 energy-dispersive detectors, but our data analysis procedure relies primarily on three of the detectors, the two detectors (at ψ = 0° and 180° in Supplemental<sup>1</sup> Fig. S2) that are positioned to record diffraction coming from planes nearly normal to the compression axis and one detector (at ψ = 90° in Supplemental<sup>1</sup> Fig. S2) that measures diffraction coming from planes that are nearly parallel to the compression axis (the transverse direction). The other detectors should produce lattice strains that are intermediate between these two end-members and confirmation of this is used as a check on data quality. Further details regarding the data analysis procedure are contained in the supplementary material. Lattice strain ( $\epsilon^{hkl}$ ) is calculated for each diffraction peak as follows:

$$\epsilon^{hkl} = \frac{(d^{hkl} - d_0^{hkl})}{d_0^{hkl}}$$

where *d*<sub>0</sub><sup>hkl</sup> is the lattice spacing measured by a given detector immediately before the beginning of deformation for each sequence.

To interpret the diffraction measurements, lattice strain vs. sample strain curves for the experiments are then compared with simulated diffraction data generated with an EPSC model (Tome and Oliver 2002). The single-crystal elastic constants used in each model were calculated for the appropriate experimental temperature and pressure from constants given in (Isaak 1992; Anderson and Isaak 1995; Abramson et al. 1997; Liu and Li 2006) and are listed in the supplementary material. Typically for olivine, we model the eight commonly observed slip systems in olivine as well as three unidirectional slip systems to simulate the formation of kink bands (Burnley 2015; Kaboli et al. 2017). For this study, we also used an additional isotropic deformation mechanism that will be discussed below. The EPSC model uses a Voce hardening law to describe the evolution of the critical resolved shear stress (τ) for each slip system with shear strain (Γ) as follows:

$$\tau = \tau_0 + (\tau_1 + \phi_1 \Gamma) \left[ 1 - e^{-\left(\frac{\phi_1 \Gamma}{\tau_1}\right)} \right]$$

where τ<sub>0</sub> is the initial critical resolved shear stress and τ<sub>1</sub>, φ<sub>0</sub>, and φ<sub>1</sub> are hardening parameters (Turner and Tome 1994; Tome and Oliver 2002). The values of τ<sub>0</sub>, τ<sub>1</sub>, φ<sub>0</sub>, and φ<sub>1</sub> used in each model are listed in Table 2.

## RESULTS

Lattice strain data vs. sample strain plots are given in Figure 1. Several key observations are worth pointing out when examining

the data. First, as is expected of stress-strain curves, the lattice strain rises sharply with sample strain at low sample strains. This behavior is generally referred to as the elastic portion of the stress-strain curve. However, with the exception of the initial portion of the 440 °C sequence, the slope of the curves deviates visibly from purely elastic behavior, as illustrated in Figure 1 by the self-consistent elastic simulations that are indicated by solid lines. The deviation from pure elastic behavior is temperature dependent with the slope deviating more at higher temperatures. Second, for each experiment, the relative difference between the lattice strains changes markedly at the yield point where the lattice strain vs. sample strain curves bend over as the sample yields (Burnley 2015; Kaboli et al. 2017). This spreading of the lattice strains can be seen in both the compressional and transverse directions. In addition, at the yield point, the internal consistency of the diffraction data, particularly in the transverse direction begins to deteriorate.

**TABLE 2.** Summary of the critical resolved shear stress ( $\tau$ ), hardening parameters ( $\tau_0$ ,  $\phi_0$ , and  $\phi_1$ ), and macroscopic stress at 3% strain for EPSC models that fit the experimental data

	$\tau$	$\tau_0$	$\phi_0$	$\phi_1$	$\sigma^a$
Sequence 1					2.42
Isotropic system <sup>b</sup>	0.2	60	60	60	
Group A: [001](100), [001]{110}, [001](010) [100](010)	0.7	0.001	0.01	0.01	
Group B: Kink system <sup>c</sup> [100]{011}	1.1	0.001	0.01	0.01	
Sequence 1 (alternative fit)					2.38
Isotropic system <sup>b</sup>	0.2	60	60	60	
Group A: [001](100), [001]{110}, [001](010) [100]{011}	0.7	0.001	0.01	0.01	
Group B: Kink system <sup>c</sup>	1.2	0.001	0.01	0.01	
Sequence 2					2.13
Isotropic system <sup>b</sup>	0.05	57	57	57	
Group A: [001](100), [001]{110}, [001](010)	0.5	0.001	0.01	0.01	
Group B: Kink system <sup>c</sup> [100]{011}	0.9	0.001	0.01	0.01	
Sequence 3					1.43
Isotropic system <sup>b</sup>	0.04	22	22	22	
Group A: [001](100), [001]{110}	0.3	0.001	0.01	0.01	
Group B: Kink system <sup>c</sup> [100]{011} [001](010)	0.6	0.001	0.01	0.01	
Sequence 4					0.63
Isotropic system <sup>b</sup>	0.01	9	9	9	
Group A: [001](100), [001]{110}	0.1	0.001	0.01	0.01	
Group B: Kink system <sup>c</sup> [100]{011} [001](010)	0.3	0.001	0.01	0.01	

Note: All units are in GPa.

<sup>a</sup> From EPSC model at 3% strain.

<sup>b</sup> Planes and directions found in Supplemental<sup>1</sup> Table S3.

<sup>c</sup> [210] on (120), [210] on (120), [504] on (405), and [504]{405} are used to simulate kink band formation.

## DISCUSSION

### Application of EPSC models

Two of the observations above have important implications for developing an EPSC model that will fit the diffraction data. The first is that a deformation mechanism that has a very low critical resolved shear stress ( $\tau_0$ ) is required in order for deformation to deviate from elastic behavior so early in the deformation experiment. In addition, this mechanism cannot accommodate very much strain or else the entire aggregate would yield completely. The second important observation is that because the lattice strains for the individual reflections remain close to each other, whatever this mechanism is, it does not differentiate between any of the measured grain populations. All of the known slip systems for olivine as well as kink band formation produce dispersion between the olivine lattice strains (Burnley 2015). Thus a new deformation mechanism that affects all grain orientations to the same degree is required to keep the lattice strains from deviating from each other.

Although the exact nature of this new deformation mechanism has not been determined, we can simulate its behavior with a “fake” slip system in the EPSC model to improve the overall fit of the models. To do this, we created a deformation mechanism for which the Schmid factor is close to 0.5 for each grain. This “slip system” consisted of planes belonging to four rhombic prisms ( $\{021\}$ ,  $\{101\}$ ,  $\{120\}$ ,  $\{301\}$ ) and two rhombic dipyramids ( $\{111\}$ ,  $\{231\}$ ) with various slip directions (full details are found in the supplementary material). This system produced the observed lack of dispersion between the measured lattice strains. The slope of the lattice strain vs. sample strain curves is adjusted using the work hardening parameters. Results of this slip system operating alone are illustrated in Supplemental<sup>1</sup> Figure S5. Once the low strain portion of the lattice strain vs. sample strain curves were successfully modeled then the slip systems typical of olivine as well as the model for kink band formation (Burnley 2015) were applied to produce the observed yielding and dispersion of the lattice strains. The inability of the models to reproduce the behavior of the (122) reflection in the second deformation sequence is probably due to issues with properly identifying the initial peak position at the start of that deformation sequence. Table 2 gives the parameters that we used to produce the model fits shown in Figure 2.

### Deriving CRSS from EPSC

In the EPSC model, the CRSS and hardening constants are treated as fitting parameters. However, if the theory behind the model is correct and the modeling process takes all the deformation mechanisms into account, then the CRSS and hardening constants should also be related to the physical processes that they describe. We, therefore, compared the CRSS for the slip component of the EPSC models, with determination of the CRSS of [100] and [001] slip from previous work by Durinck et al. (2007) (Fig. 3). Durinck et al. (2007) compiled experimental data on the CRSS of olivine slip systems measured at low pressure in single-crystal studies and then parameterized the CRSS as a function of temperature. The dashed lines in Figure 3 show the range of CRSS as a function of temperature as indicated by the uncertainty in their parameterization. Some of our models required that different CRSS be used for different slip planes that have the same Burger’s vector; in this case, a weighted average was used in Figure 3. In the case of

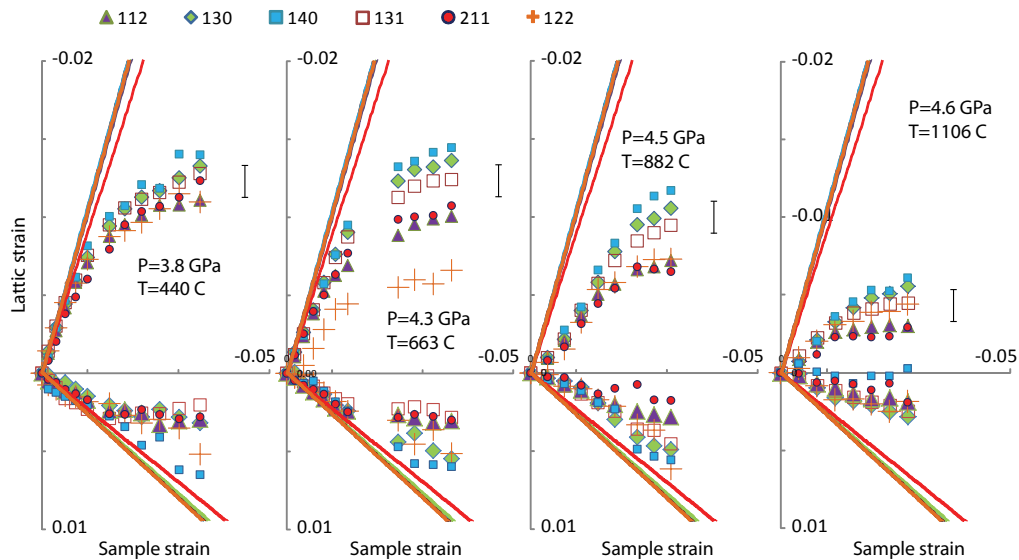


**FIGURE 1.** Lattice strain vs. sample strain data (symbols) for the four deformation sequences. The solid lines show the self-consistent elastic model for each lattice plane calculated for the pressure and temperature conditions of each sequence. The uncertainty in lattice strain is  $\pm 0.001$ , which is illustrated by an error bar placed to the right side of each deformation sequence.

[100] slip at 440 °C, we found two EPSC models that were indistinguishable in terms of their fit to the experimental data, which had different CRSS (Table 2). This variation in CRSS is indicated by plotting a symbol for each model value and using a larger error bar. It is important to keep in mind that our CRSS values were determined at high pressure and that the CRSS for slip, especially along [100] should be somewhat higher (Durinck et al. 2005) than

at low pressure. Differences in composition between forsterite and San Carlos olivine were ignored by (Durinck et al. 2007), but this small difference in chemistry has not been observed to have a large impact on the slip (Bollinger et al. 2012, 2015). Keeping in mind the pressure difference, the match between the CRSS for [001] slip from our models as compared to that from previous work is remarkable considering the difference in the experimental

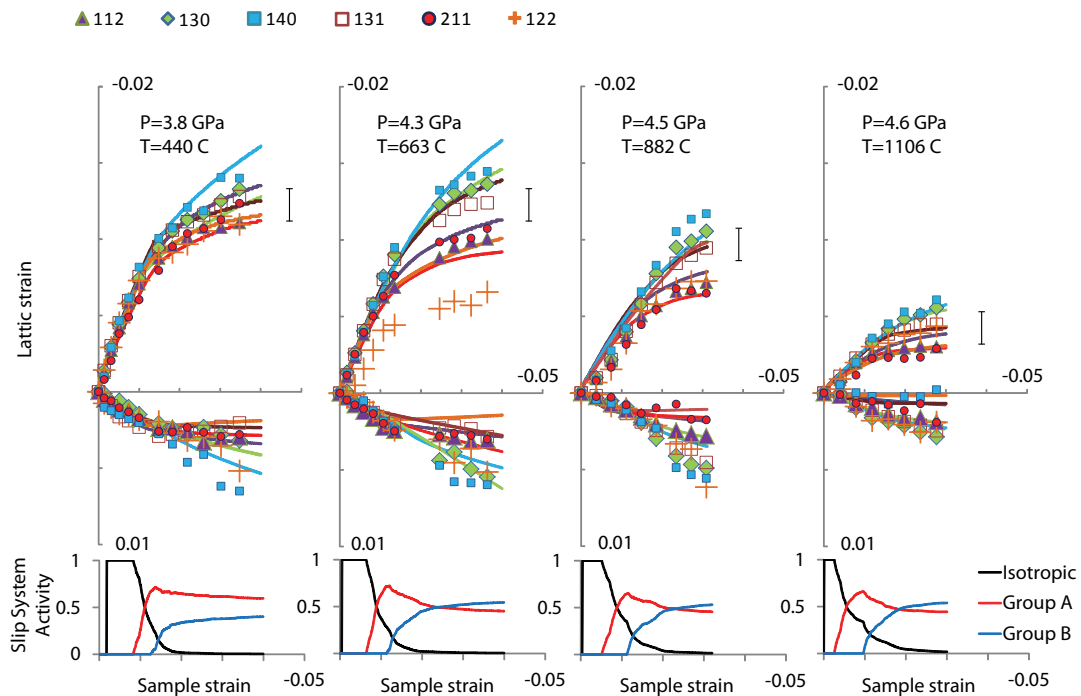


**FIGURE 2.** Lattice strain vs. sample strain data (symbols) for the four deformation sequences. The lines show the self-consistent models calculated to match the data. The slip system activity is plotted below each. The slip systems included in each group are listed in Table 2. The uncertainty in lattice strain is  $\pm 0.001$ , which is illustrated by an error bar placed to the right side of each deformation sequence.

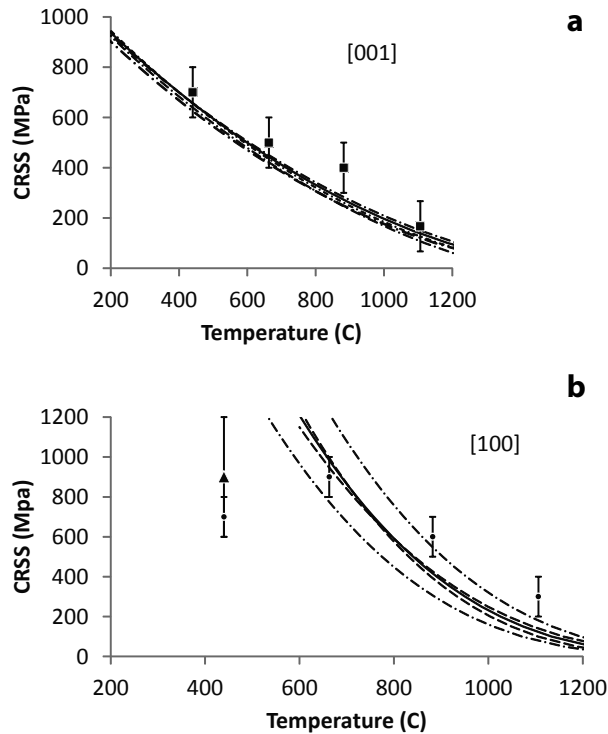


**FIGURE 3.** CRSS of slip as a function of temperature for (a) [001] and (b) [100] slip. The data points (symbols) are derived from the CRSS listed in Table 2. The dashed lines indicate various parameterizations taken from (Durinck et al. 2007), based on the upper and lower bound of each parameter given by that study.

techniques used to determine the CRSS. It is interesting to note that the parameterization from (Durinck et al. 2007) gives a CRSS for [100] slip between 1550 and 2250 MPa at 440 °C that is not consistent with our models, which require some slip on [100]. However, it should be noted that this parameterization is based on only five experimental data points below 1000 °C, which offers little constraint at low temperature.

#### Inelastic behavior at low strain

While the isotropic slip system that we used in the EPSC models was useful to describe the physical phenomena that we observed, it is just a “hack”, and the input parameters (e.g., CRSS and hardening parameters) do not have a direct physical meaning. A more meaningful description of the phenomena is to calculate the apparent value of the Young’s modulus for each temperature and compare that to the Young’s modulus as derived from single-crystal elasticity (Fig. 4).

Although additional studies are required, we suggest that the physical process that is operating at low strain could be grain boundary sliding accommodated either elastically or by dislocation glide. The theory of elasticity of polycrystals with viscous grain boundaries was developed by (Zener 1941) who showed that the apparent elastic modulus reduction caused by relaxation on grain boundaries is a function of the viscosity of the grain boundaries, which is, in turn, a function of temperature. The decrease in the apparent Young’s modulus as a function of temperature that we observe is similar to that observed in metals (e.g., Ke 1947;

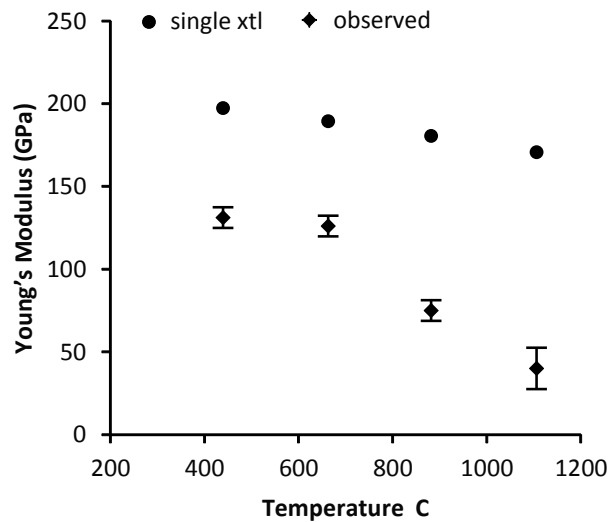


**FIGURE 4.** Plot of the apparent Young’s modulus from the initial portion of each deformation sequence compared with the Young’s modulus as calculated from the single-crystal elastic constants.

~20%) but of a greater magnitude. Displacement along grain boundaries in olivine aggregates has been directly observed in high-temperature deformation experiments (1200–1300 °C) (Maruyama and Hiraga 2017a, 2017b) and dislocation assisted grain boundary sliding is widely understood to be an important deformation process for high-temperature flow of olivine (Hirth and Kohlstedt 1995a, 1995b; Dimanov et al. 2011; Hansen et al. 2011; Hansen et al. 2012; Tielke et al. 2016). Elastically accommodated grain boundary sliding is thought to be an important process in the anelastic behavior of the mantle (Cooper 2002; Sundberg and Cooper 2010). At present, work on grain boundary sliding as a deformation mechanism in olivine aggregates has been confined to low pressure. Thus these observations may point to a means of using the D-DIA apparatus to study the effect of pressure on grain boundary sliding.

#### IMPLICATIONS

The results of this project have several implications both for the improved utility of using elastic plastic self-consistent (EPSC) models to better interpret in situ diffraction data from deformation experiments as well as understanding the deformation processes occurring in the experiment. First, the fact that we can reproduce the critical resolved shear stresses (CRSS) for [001] and [100] slip from single-crystal experiments argues that polycrystalline deformation experiments analyzed with an EPSC model that achieves a good match to the diffraction may be a good way to measure CRSS under conditions where single-crystal deformation experiments are more challenging. Second, the observation of low strain inelastic behavior points to several interesting avenues for future research. Although this deformation mechanism does not produce substantial bulk strain, it will play a role in the distribution of stress throughout the aggregate and is, therefore, an important part of the aggregate’s deformation history. In addition, as suggested above, the D-DIA can be used to study the effect of pressure on this deformation mechanism and determine its importance in the Earth’s mantle.

## FUNDING

This research was sponsored in part by the National Nuclear Security Administration under the Stewardship Science Academic Alliances program through DOE Cooperative Agreement no. DE-NA0001982, and by the National Science Foundation under award NSF-EAR13613399 and NSF-EAR1417218. Use of the Advanced Photon Source, Argonne National Laboratory, is supported by DOE-BES, under Contract No. DE-AC02-06CH11357. Operation of the D-DIA at Sector 6BMB is supported by the Consortium for Materials Properties Research in Earth Sciences under NSF cooperative agreement EAR 11-57758.

## ACKNOWLEDGMENTS

We thank Dawn Reynoso for assistance with data analysis as well as Haiyan Chen for assistance on the beamline.

## REFERENCES CITED

- Abramson, E.H., Brown, J.M., Slutsky, L.J., and Zaug, J. (1997) The elastic constants of San Carlos olivine to 17 GPa. *Journal of Geophysical Research*, 102(B6), 12,253–12,263.
- Agnew, S.R., Brown, D.W., and Tome, C.N. (2006) Validating a polycrystal model for the elastoplastic response of magnesium alloy AZ31 using in situ neutron diffraction. *Acta Materialia*, 54(18), 4841–4852.
- Anderson, O.L., and Isaak, D.G. (1995) Elastic constants of mantle minerals at high temperatures. In T.J. Ahrens, Ed., *Mineral Physics and Crystallography: A Handbook of Physical Constants (Reference Shelf 2)*, p. 64–97. American Geophysical Union, Washington, D.C.
- Bollinger, C., Merkel, S., and Raterron, P. (2012) In situ quantitative analysis of stress and texture development in forsterite aggregates deformed at 6 GPa and 1373 K. *Journal of Applied Crystallography*, 45, 263–271.
- Bollinger, C., Merkel, S., Cordier, P., and Raterron, P. (2015) Deformation of forsterite polycrystals at mantle pressure: Comparison with Fe-bearing olivine and the effect of iron on its plasticity. *Physics of the Earth and Planetary Interiors*, 240, 95–104.
- Burnley, P.C. (2015) Modeling of plastic deformation in fayalite olivine. *American Mineralogist*, 100, 1424–1433.
- Burnley, P.C., and Zhang, D. (2008) Interpreting in situ X-ray diffraction data from high pressure deformation experiments using elastic-plastic self-consistent models: an example using quartz. *Journal of Physics: Condensed Matter*, 20(28), 10 pp.
- Cooper, R.F. (2002) Seismic wave attenuation: Energy dissipation in viscoelastic crystalline solids. In S. Karato and H.R. Wenk, Eds., *Plastic Deformation of Minerals and Rocks*, 51, p. 253–290. Reviews in Mineralogy, Mineralogical Society of America, Chantilly, Virginia.
- Dimanov, A., Raphanel, J., and Dresen, G. (2011) Newtonian flow of heterogeneous synthetic gabbros at high strain: Grain sliding, ductile failure, and contrasting local mechanisms and interactions. *European Journal of Mineralogy*, 23(3), 303–322.
- Durham, W.B., Weidner, D.J., Karato, S.I., and Wang, Y.B. (2002) New developments in deformation experiments at high pressure. In S. Karato and H.R. Wenk, Eds., *Plastic Deformation of Minerals and Rocks*, 51, 21–49. Reviews in Mineralogy, Mineralogical Society of America, Chantilly, Virginia.
- Durham, W.B., Mei, S., Kohlstedt, D.L., Wang, L., and Dixon, N.A. (2009) New measurements of activation volume in olivine under anhydrous conditions. *Physics of the Earth and Planetary Interiors*, 172(1–2), 67–73.
- Durinck, J., Legris, A., and Cordier, P. (2005) Pressure sensitivity of olivine slip systems: First-principle calculations of generalised stacking faults. *Physics and Chemistry of Minerals*, 32, 646–654.
- Durinck, J., Devincere, B., Kubin, L., and Cordier, P. (2007) Modeling the plastic deformation of olivine by dislocation dynamics simulations. *American Mineralogist*, 92, 1346–1357.
- Hansen, L.N., Zimmerman, M.E., and Kohlstedt, D.L. (2011) Grain boundary sliding in San Carlos olivine: Flow law parameters and crystallographic-preferred orientation. *Journal of Geophysical Research: Solid Earth*, 116, 16 pp.
- (2012) The influence of microstructure on deformation of olivine in the grain-boundary sliding regime. *Journal of Geophysical Research: Solid Earth*, 117, 17 pp.
- Hilairet, N., Wang, Y.B., Sanehira, T., Merkel, S., and Mei, S.M. (2012) Deformation of olivine under mantle conditions: An in situ high-pressure, high-temperature study using monochromatic synchrotron radiation. *Journal of Geophysical Research: Solid Earth*, 117, 16 pp.
- Hirth, G., and Kohlstedt, D.L. (1995a) Experimental constraints on the dynamics of the partially molten upper-mantle 2. Deformation in the dislocation creep regime. *Journal of Geophysical Research: Solid Earth*, 100(B8), 15,441–15,449.
- (1995b) Experimental constraints on the dynamics of the partially molten upper-mantle—Deformation in the diffusion creep regime. *Journal of Geophysical Research: Solid Earth*, 100(B2), 1981–2001.
- Isaak, D.G. (1992) High-temperature elasticity of iron-bearing olivines. *Journal of Geophysical Research*, 97(B2), 1871–1885.
- Jain, C., Korenaga, J., and Karato, S.-i. (2017) On the yield strength of oceanic lithosphere. *Geophysical Research Letters*, 44, 9716–9722.
- Kaboli, S., and Burnley, P.C. (2017) ECCI, EBSD and EPSC characterization of rhombohedral twinning in polycrystalline  $\alpha$ -alumina deformed in the D-DIA apparatus. *Journal of Applied Crystallography*, 50, 1691–1704.
- Kaboli, S., Burnley, P.C., Xia, G., and Green, H.W. II (2017) Pressure dependence of creep in forsterite olivine: comparison of measurements from the D-DIA and Griggs apparatus. *Geophysical Research Letters*, 44, 10,939–10,947. <https://doi.org/10.1002/2017GL075177>
- Ke, T.-S. (1947) Experimental evidence of the viscous behavior of grain boundaries in metals. *Physical Review Letters*, 71(8), 533–546.
- Li, L., Weidner, D.J., Chen, J.H., Vaughan, M.T., Davis, M., and Durham, W.B. (2004) X-ray strain analysis at high pressure: Effect of plastic deformation in MgO. *Journal of Applied Physics*, 95(12), 8357–8365.
- Liu, W., and Li, B. (2006) Thermal equation of state of  $(\text{Mg}_{0.9}\text{Fe}_{0.1})_2\text{SiO}_4$  olivine. *Physics of the Earth and Planetary Interiors*, 157(3), 188–195.
- Maruyama, G., and Hiraga, T. (2017a) Grain- to multiple-grain-scale deformation processes during diffusion creep of forsterite plus diopside aggregate: 1. Direct observations. *Journal of Geophysical Research: Solid Earth*, 122(8), 5890–5915.
- (2017b) Grain- to multiple-grain-scale deformation processes during diffusion creep of forsterite plus diopside aggregate: 2. Grain boundary sliding-induced grain rotation and its role in crystallographic preferred orientation in rocks. *Journal of Geophysical Research: Solid Earth*, 122(8), 5916–5934.
- Mei, S., Suzuki, A.M., Kohlstedt, D.L., Dixon, N.A., and Durham, W.B. (2010) Experimental constraints on the strength of the lithospheric mantle. *Journal of Geophysical Research: Solid Earth*, 115, 9 pp.
- Merkel, S., Tome, C., and Wenk, H.-R. (2009) Modeling analysis of the influence of plasticity on high pressure deformation of hcp-Co. *Physical Review B*, 79(6).
- Raterron, P., Merkel, S., and Holyoke, C.W. III (2013) Axial temperature gradient and stress measurements in the deformation-DIA cell using alumina pistons. *Review of Scientific Instruments*, 84(4), 11 pp.
- Schneider, C.A., Rasband, W.S., and Eliceiri, K.W. (2012) NIH Image to ImageJ: 25 years of image analysis. *Nature Methods*, 9, 671–675.
- Singh, A.K., Balasingh, C., Mao, H.K., Hemley, R.J., and Shu, J.F. (1998) Analysis of lattice strains measured under nonhydrostatic pressure. *Journal of Applied Physics*, 83(12), 7567–7575.
- Sundberg, M., and Cooper, R.F. (2010) A composite viscoelastic model for incorporating grain boundary sliding and transient diffusion creep: correlating creep and attenuation responses for materials with a fine grain size. *Philosophical Magazine*, 90(20), 2817–2840.
- Tielke, J.A., Hansen, L.N., Tasaka, M., Meyers, C., Zimmerman, M.E., and Kohlstedt, D.L. (2016) Observations of grain size sensitive power law creep of olivine aggregates over a large range of lattice-preferred orientation strength. *Journal of Geophysical Research: Solid Earth*, 121(2), 506–516.
- Tome, C.N., and Oliver, E.C. (2002) Code Elasto-plastic self-consistent (EPSC). Los Alamos National Laboratory, New Mexico.
- Turner, P.A., and Tome, C.N. (1994) A study of residual-stresses in ZIRCALOY-2 with rod texture. *Acta Metallurgica et Materialia*, 42(12), 4143–4153.
- Turner, P.A., Christodoulou, N., and Tome, C.N. (1995) Modeling the mechanical response of rolled zircaloy-2. *International Journal of Plasticity*, 11(3), 251–265.
- Vaughan, M., Chen, J., Li, L., Weidner, D.J., and Li, B. (2000) Use of X-ray imaging techniques at high pressure and high temperature for strain measurements. In M.H. Manghnani, W.J. Nellis, and M.F. Nicol, Eds., *Science and Technology of High Pressure Proceedings of AIRAPT-17*, p. 1097–1098. Universities Press, Hyderabad.
- Wang, Y.B., Durham, W.B., Getting, I.C., and Weidner, D.J. (2003) The deformation-DIA: A new apparatus for high temperature triaxial deformation to pressures up to 15 GPa. *Review of Scientific Instruments*, 74(6), 3002–3011.
- Weidner, D.J., and Li, L. (2006) Measurement of stress using synchrotron X-rays. *Journal of Physics: Condensed Matter*, 18(25), S1061–S1067.
- Weidner, D.J., Wang, Y., Chen, G., Ando, J., and Vaughan, M.T. (1998) Rheology measurements at high pressure and temperature. In M.H. Manghnani and T. Yagi, Eds., *Properties of Earth and Planetary Materials at High Pressure and Temperature*, p. 173–482. AGU, Washington, D.C.
- Weidner, D.J., Vaughan, M.T., Wang, L.P., Long, H.B., Li, L., Dixon, N.A., and Durham, W.B. (2010) Precise stress measurements with white synchrotron X-rays. *Review of Scientific Instruments*, 81(1), 5 pp.
- Zener, C. (1941) Theory of the elasticity of polycrystals with viscous grain boundaries. *Physical Review*, 60(12), 906–908.

MANUSCRIPT RECEIVED JUNE 1, 2018

MANUSCRIPT ACCEPTED NOVEMBER 2, 2018

MANUSCRIPT HANDLED BY SYLVIE DEMOUCHE

## Endnote:

<sup>1</sup>Deposit item AM-19-26666, Supplemental Material. Deposit items are free to all readers and found on the MSA website, via the specific issue's Table of Contents (go to [http://www.minsocam.org/MSA/AmMin/TOC/2019/Feb2019\\_data/Feb2019\\_data.html](http://www.minsocam.org/MSA/AmMin/TOC/2019/Feb2019_data/Feb2019_data.html)).